Journal of the Mechanics and Physics of Solids 59 (2011) 1858–1871

Contents lists available at ScienceDirect

Journal of the Mechanics and Physics of Solids

journal homepage: www.elsevier.com/locate/jmps

Atomistic insights into dislocation-based mechanisms of void growth and coalescence

Changwen Mi [a,b,*], Daniel A. Buttry [c], Pradeep Sharma [d], Demitris A. Kouris [e]

[a] Jiangsu Key Laboratory of Engineering Mechanics, Southeast University, Nanjing, Jiangsu 210096, China
[b] Department of Engineering Mechanics, Southeast University, Nanjing, Jiangsu 210096, China
[c] Department of Chemistry and Biochemistry, Arizona State University, Tempe, AZ 85287, USA
[d] Department of Mechanical Engineering, University of Houston, Houston, TX 77204, USA
[e] College of Science and Engineering, Texas Christian University, Fort Worth, TX 76129, USA

ARTICLE INFO

Article history:
Received 4 June 2010
Received in revised form
12 May 2011
Accepted 19 May 2011
Available online 26 May 2011

Keywords:
Void cavitation
Dislocations
Crystal plasticity
Atomistic simulations

ABSTRACT

One of the low-temperature failure mechanisms in ductile metallic alloys is the growth of voids and their coalescence. In the present work we attempt to obtain atomistic insights into the mechanisms underpinning cavitation in a representative metal, namely Aluminum. Often the pre-existing voids in metallic alloys such as Al have complex shapes (e.g. corrosion pits) and the defromation/damage mechanisms exhibit a rich size-dependent behavior across various material length scales. We focus on these two issues in this paper through large-scale calculations on specimens of sizes ranging from 18 thousand to 1.08 million atoms. In addition to the elucidation of the dislocation propagation based void growth mechanism we highlight the observed length scale effect reflected in the effective stress–strain response, stress triaxiality and void fraction evolution. Furthermore, as expected, the conventionally used Gurson's model fails to capture the observed size-effects calling for a mechanistic modification that incorporates the mechanisms observed in our (and other researchers') simulation. Finally, in our multi-void simulations, we find that, the splitting of a big void into a distribution of small ones increases the load-carrying capacity of specimens. However, no obvious dependence of the void fraction evolution on void coalescence is observed.

1. Introduction

Metallic alloys such as high strength aluminum alloys typically contain concentrations of secondary metallic phases that are above their saturation solubility. The precipitates of intermetallic particles are the often primary sources of structural susceptibility-certainly the case for Al alloys (Dufek et al., 2007). The dealloying of intermetallic particles results in voids and pits. Aluminum and other similar metals generally fail by growth and coalescence of voids and pits, mechanically (Mcclintock et al., 1966; Tvergaard, 1990) and electrochemically (Fontana, 1986). Extensive continuum (Gurson, 1977; Tvergaard, 1990; van der Giessen and Tvergaard, 1990; Tvergaard and Needleman, 1995; Onck and van der Giessen, 1999; Shen, 2004; Zhao and Chen, 2008; Scheyvaerts et al., 2011) and atomistic studies (Belak and Minich, 1998; Gullett et al., 2004; Potirniche et al., 2006; Traiviratana et al., 2008; Rudd et al., 2007; Rudd, 2009) have been carried out to investigate the progressive expansion of voids and the generation of new vacancies, under an increased level of effective stress.

* Corresponding author at: Jiangsu Key Laboratory of Engineering Mechanics, Southeast University, Nanjing, Jiangsu 210096, China.
E-mail address: mi@seu.edu.cn (C. Mi).

0022-5096/$ - see front matter © 2011 Elsevier Ltd. All rights reserved.
doi:10.1016/j.jmps.2011.05.008

Two primary mechanisms that have been proposed are vacancy condensation (Cuitino and Ortiz, 1996) and dislocation emissions (Lubarda et al., 2004; Traiviratana et al., 2008; Lubarda, 2011). The applicability of these two models is governed by factors such as temperature, strain rates and the localization of plastic flow. Under the conditions of low temperature and high strain rates, Lubarda et al. (2004), Lubarda (2011) and Traiviratana et al. (2008) have proposed that dislocation emissions from void fronts due to high stress concentrations are the dominant mechanism of void expansion. According to their thesis, both prismatic and shear dislocation loops serve as a vehicle to radially transport atoms away from void fronts and result in the further cavitation of porous materials. Existing voids expand as dislocation loops propagate away from the void front. Void expansion is further enhanced at the later stage of deformation due to the coalescence of previously isolated vacancies and voids. Void expansion substantially reduces the stress resistivity of ductile metals and greatly softens the material. Although the ability to carry load can be increased by a certain amount due to dislocation reactions, the continuous void expansion is an unstoppable process under increasing external forces, until the ultimate deterioration of the material.

The involvement of shear dislocation loops in void growth mechanisms as proposed by Lubarda et al. (2004) and Traiviratana et al. (2008) has been challenged by Bulatov et al. (2010) and there is an apparent disagreement between two groups of researchers on this issue (Bringa et al., 2010). We will comment on this in Section 3.3.

Among all the previous studies related to void growth and coalescence the void geometry has been limited to either spheres (Marian et al., 2004; Traiviratana et al., 2008) or cylinders (Gullett et al., 2004; Potirniche et al., 2006) due to their simplicity. In practical situations, however, void shapes can be much more complicated. A particular type of void, namely corrosion pits, can be seen as an one-dimensional non-through defect whose depth is usually equivalent to or even longer than its diameter. In this study, we propose void geometries similar to that of an one-end capped nanotube, as shown in Fig. 1, to mimic such a pit. The central goal of this work is to perform a systematic study of the void expansion and coalescence by dislocation pattern and length scale analyses. Molecular dynamics simulations with EAM potentials are employed to investigate the elastoplastic deformation and ductile deterioration of monocrystalline aluminum at the nanoscale. A uniaxial strain up to 20% is applied on all three types of specimens that contain one, two and five nanovoids, respectively. The number of atoms for each type of specimen ranges from several tens of thousands to over a million, involving four material lengths.

The paper is organized as follows: several macroscopic quantities including the effective stress–strain response, stress triaxiality, and void fraction are calculated from the atomistic simulations to provide the fundamental data analysis aiming

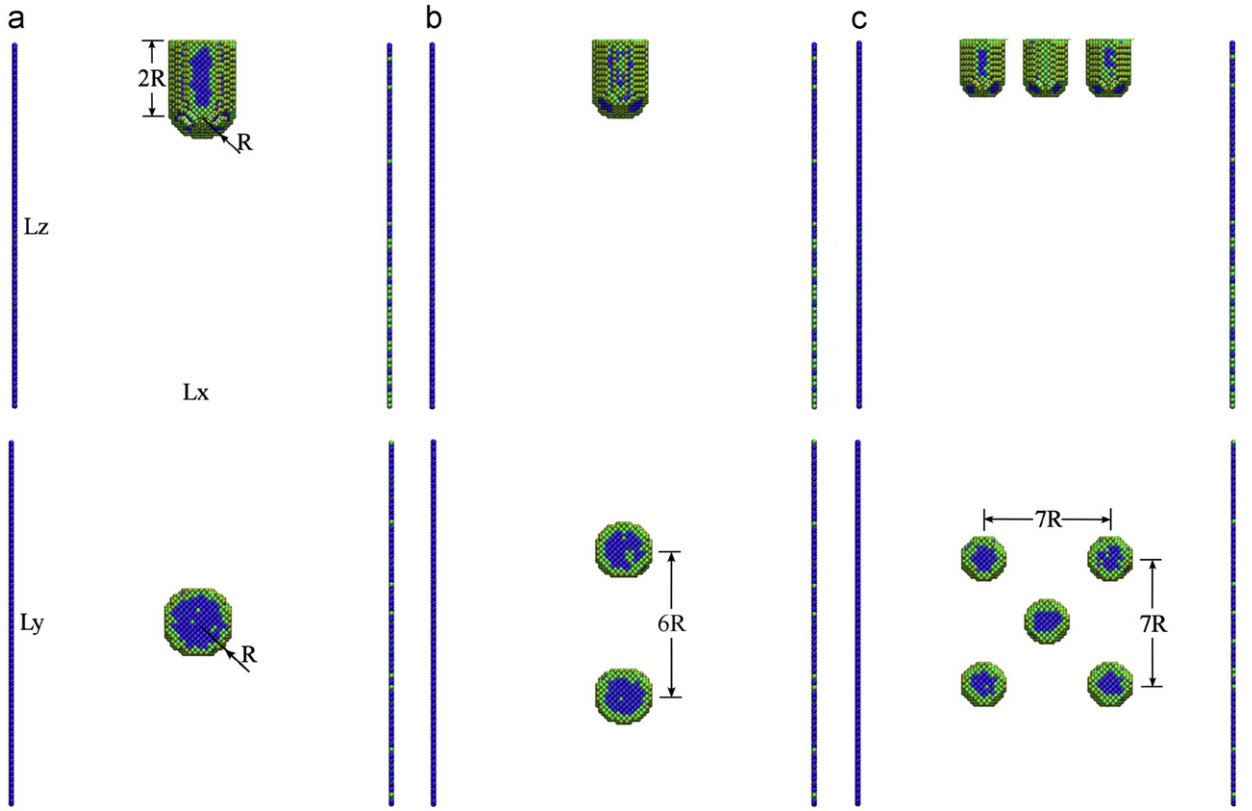

Fig. 1. Void geometry and distributions of (a) one-void, (b) two-void and (c) five-void models listed in Table 1. The Schematic is generated from the equilibrated configuration of the largest run of each model. A constant void volume fraction of 0.5% results in different void sizes (R) for specimens with different number of voids based on Eq. (4). The two vertical planes of atoms represent the rigid layers upon which a uniaxial tension is applied under a constant strain rate of 2×10^8 s^{-1}.

to elucidate length scale effects (Section 2). Dislocation patterns emitted from the void front under plastic strains are analyzed in detail in terms of the centro-symmetry deviation parameter (Kelchner et al., 1998) (Section 2). In Section 3, we focus on the length scale analysis of void growth and coalescence as well as the morphological evolution of void geometries via dislocation analysis. Discussion and a few concluding remarks resulting from the atomistic simulations, particularly in light of recent controversy regarding void growth mechanisms, are presented in Section 4.

2. Description of the atomistic simulations

We performed the atomistic simulations using the large-scale atomic/molecular massively parallel simulator (LAMMPS) that was developed by Plimpton (1995), at Sandia National Laboratories. The interatomic interactions of face-centered cubic aluminum structure were simulated by an EAM (Daw and Baskes, 1983, 1984; Foiles et al., 1986) potential developed by Mishin et al. (1999) due to its accuracy in simulating crystalline defects in bulk aluminum. All EAM potential functions share a common mathematical form of interatomic interactions. Namely, the total energy of a system of particles is expressed by

$$E_{tot}=\sum_i\left\{F_i(\rho_i)+\frac{1}{2}\sum_{j\neq i}\phi_{ij}(r_{ij})\right\}, \tag{1}$$

where ϕ_{ij} is the conventional pairwise potential term given as a function of the separation distance r_{ij} between atoms i and j. $F_i(\rho_i)$ is the energy required to embed an atom at site i having a background electron density ρ_i and ρ_i is a linear superposition of the atomic electron densities f_j due to all atoms interacting with i

$$\rho_i=\sum_{j\neq i}f_j(r_{ij}). \tag{2}$$

In the above equations, the Roman subscripts refer to atomic indices and no summation should be assumed when repeated. The adjustable parameters in the EAM potential are fitted to both an experimental database and a large set of of structural energies generated by the first-principles linearized augmented plane-wave (LAPW) method (Andersen, 1975; Wei and Krakauer, 1985). The inclusion of the vacancy formation and migration energy is crucial for the simulation of void cavitation in bulk aluminum due to their similar local atomic environment.

To quantify and visualize the dislocation structures, the coordination number (Li et al., 2002), the slip vector (Zimmerman et al., 2001) and the centro-symmetry deviation parameter (Kelchner et al., 1998) are widely used in the literature. We practically calculated all three parameters and found that the atomic coordination number and the slip vector become sensitive to atomic thermal vibrations at elevated temperatures (Pei et al., 2007). Furthermore, the slip vector analysis always needs a reference configuration so that we can calculate the relative displacement among atoms between snapshots and hence is computationally expensive. More importantly, it does not allow for identification of crystal defects that are not generated from atomic motion such as surfaces, grain boundaries, vacancies and voids. Based on these arguments, the centro-symmetry deviation parameter has been chosen to characterize the plastic deformation in the present work. In a centro-symmetric lattice, every atom is a center of inversion symmetry of the whole lattice. For any neighbor of a given atom at position $\mathbf{r}$, there always exists another neighbor at position $-\mathbf{r}$. These two neighbors form a centro-symmetric pair about the atom of interest. The centro-symmetry deviation parameter provides a quantitative measure of the deviation of a given atom's local structure from its ideal centro-symmetry, up to the nearest neighbors (Kelchner et al., 1998):

$$P=\sum_{i=1}^{6}|\mathbf{R}_i+\mathbf{R}_{i+6}|^2, \tag{3}$$

where $\mathbf{R}_i$ is the position vector pointing from the central atom to one of its nearest neighbors with index i. $i+6$ refers to the index of another neighbor, which forms the closest centro-symmetric pair about the central atom with the neighbor i. Here, "closest centro-symmetric pair" means that the magnitude of the position vector sum of the pair atoms is one of the six smallest among all the sums constructed from two arbitrary neighbors. An algorithm for the calculation of the centro-symmetry deviation parameter can be summarized as:

1. Find the 12 nearest neighbors for atoms of interest. Generally we will have more than 12 neighbors, but only the 12 nearest ones are needed. For atoms close to defects, i.e. on a free surface or around vacancies, the cutoff distance needs to be increased to include at least 12 neighbors.
2. Calculate the magnitude of vector sums for all 66 distinct pairs of atoms formed by the selected 12 neighbors.
3. Sort the array of 66 entries in an ascending order.
4. The centro-symmetry deviation parameter is taken as the sum of squares of the first 6 entries of the sorted list.

The centro-symmetry deviation parameter is zero for perfect fcc atoms, $3a^2/2$ or a^2 for atoms on a $\{0\,0\,1\}$ free surface, $3a^2/2$ for atoms on an $\{1\,1\,1\}$ free surface, $a^2/2$ for atoms in an intrinsic stacking fault and a $\{1\,1\,1\}\langle 0\,1\,\bar{1}\rangle$ perfect dislocation core and $a^2/3$ for atoms at an $\{1\,1\,1\}\langle 1\,1\,\bar{2}\rangle$ partial dislocation core, with a denoting the lattice constant.

Table 1
Summary of the geometric parameters for the four cases of each of the three models shown in Fig. 1. The units of L_x, L_y, L_z and R are nm.

Case	L_x	$L_y = L_z$	R (one-void)	R (two-void)	R (five-void)	Atoms
1	7.29	6.48	0.55	0.43	0.32	18 K
2	13.77	12.96	1.09	0.86	0.64	140 K
3	20.25	19.44	1.64	1.30	0.96	463 K
4	26.73	25.92	2.18	1.73	1.28	1.08 M

Considering the widely separated values of the centro-symmetry deviation parameters, different atomic defects can be easily distinguished.

Rectangular domains of single crystal aluminum, with crystalline axes $x=[1\ 0\ 0]$,$y=[0\ 1\ 0]$ and $z=[0\ 0\ 1]$, were created with atoms in perfect fcc lattice sites. Three models, each with four cases of increasing domain sizes, are considered in this study and summarized in Table 1. The number of atoms for these cases varies from 10^4 to 10^6. A defect structure containing a number of voids is distributed about the center of the top surface ($z=0$) of the simulation box. The geometry and distribution of voids for the three models are shown in Fig. 1. To study the effect of void distribution on the plastic deformation, a constant initial volume fraction of 0.5% is used according to the formula:

$$V_f = (\tfrac{8}{3}\pi R^3 N)/V, \tag{4}$$

where R is the void size, N is the number of voids and V denotes the total volume of the simulation box. The calculated void sizes are tabulated in Table 1 for different models and runs.

Before the domain is subjected to any load, the simulation is performed for 50 ps under a constant, low temperature of 5 K for equilibration. Periodic boundary conditions are applied in the y and z direction with a periodicity, L_y and L_z. A uniaxial expansion strain up to 20% along the x direction is applied by freezing one-unit cell of atoms at the $-x$ boundary and imposing a constant strain rate of $2\times10^8\ \mathrm{s}^{-1}$ on another one-unit cell of atoms at the $+x$ boundary. Newton's equation of motion for both the equilibration and straining process is integrated with a timestep of 1 fs. The velocity component along the loading direction for all mobile atoms, i.e. those in between the frozen boundary ones, is ramped according to their x coordinate to avoid the initial shock wave that may be induced by strains. Thermostating can be non-trivial in molecular dynamics simulations and special care is required (Jang et al., 2007). In the present study all three velocity components of mobile atoms are thermostated during equilibration; velocity component along the loading (x) direction, however, is excluded during straining.

When properly averaged over time and space, the virial stress tensor (see Admal and Tadmor, 2010 for a deep discussion of various measures of atomistic stress tensor) represents one of the microscopic measures of the continuum Cauchy stress in molecular dynamics. The work of Admal and Tadmor (2010) suggests other measures of atomistic stress that may be more appropriate, however, in this paper we have chosen the virial definition and do not expect any changes in our conclusions as a result of this choice. In terms of the EAM potential functions (1) and (2), for a system of interacting atoms, the virial stress tensor can be defined as

$$\sigma_{\alpha\beta} = \sum_i \frac{1}{\Omega_i}\left\{-m_i v_{i\alpha} v_{i\beta} + \sum_{j\neq i}\left[\left(\frac{dF_i}{d\rho_i}\frac{df_j}{dr_{ij}} + \frac{1}{2}\frac{d\phi_{ij}}{dr_{ij}}\right)\frac{r_{ij\alpha} r_{ij\beta}}{r_{ij}}\right]\right\}, \tag{5}$$

where Ω_i denotes the atomic volume of atom i, m_i and v_i are the corresponding atomic mass and velocity, and the Greek indices α and β represent the Cartesian coordinate axes and assume values from 1 to 3. The stress tensor includes contributions of the instantaneous atomic velocities due to thermal vibrations and the interatomic forces. While the second term is the sole contribution in static simulations (energy minimizations), the first term comprises an integral part of the virial stress tensor for dynamics simulations at a finite temperature, as shown by Subramaniyan and Sun (2008).

In the region near the void defects, the reduced y–z cross sectional area leads to higher stresses. This increase of stress does not correspond to a measurable macroscopic stress at the continuum level. It is an artificial result of atomic scale geometry. To avoid the unfavorable stress increase, an averaging of stresses is taken over atoms in regions far away from defects, $|x|\geq 2R$, $3R$ and $7R$ for the one-void, two-void and five-void models, respectively. Furthermore, due to the way of thermostating in our simulations, the velocity component along the loading direction is excluded in the stress calculation Eq. (5).

Mcclintock et al. (1966) demonstrated that the failure of ductile metals is promoted by the nucleation, growth and coalescence of voids. Thus it becomes important to characterize the time evolution of void fraction such that its connections with the stress–strain behavior and dislocation formations can be correlated. Here we adapt a void fraction calculation algorithm developed by Gullett et al. (2004). Firstly, we discretize the simulation domain into a simple orthorhombic grid of cells. The size of the cells is at least equal to the equilibrium distance among nearest aluminum neighbors (≥ 0.2864 nm). To increase the computational efficiency, the side-length of grid cells may vary with increasing simulation box sizes among cases. With the increase of L_x during the straining process, the x side-length of grid cells changes from timestep to timestep in order to accommodate an integral number of cells along the x direction. The side-lengths along the other two directions are fixed

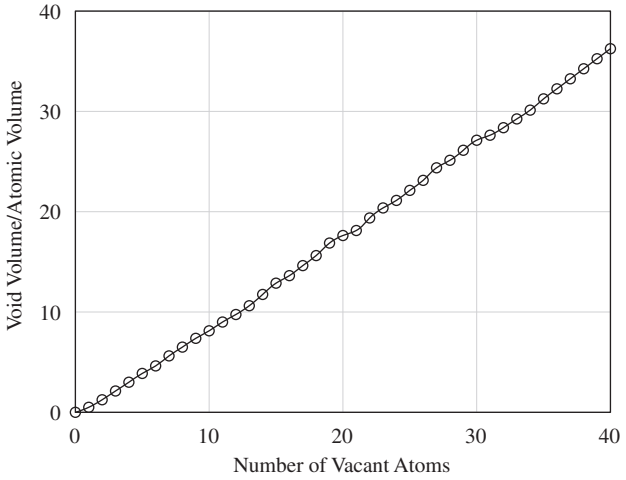

Fig. 2. Validation of void growth algorithm.

throughout the simulations due to their periodicities. The volume of solid is then obtained as the sum of the volumes of cells containing at least one atom, while that of a void is obtained as the total volume of empty cells within the boundaries of the simulation box. This way, the volume fraction is simply the ratio of the number of empty cells over the total number of cells.

The void fraction algorithm is tested by calculating the void volume of a cubic box of perfect aluminum lattice containing various number of connected vacancies. Fig. 2 shows the calculated void volume, normalized by the equilibrium atomic volume of aluminum ($\approx 16.6075\,\text{A}^3$), as a function of the number of vacant atoms. It is seen that the result of the present algorithm is in reasonable agreement with the exact solution of the problem (straight diagonal line, not shown in Fig. 2).

In general, deformation of ductile metals exhibits a well defined elastic region and a plastic one, separated by a yield point, at which the linear or quasi-linear stress–strain relationship ends. Elastic deformation is recoverable and in general also compressible. However, due to the marginal effect of elastic deformation on void volume evolution in our simulation, the void volume fraction can be approximated as a constant during the elastic stage: $V_f=(V-V_S)/V=f_0$ with V_S and V denoting, respectively, the volume of the solid and of the whole system. In contrast, plastic deformation is permanent and produced by volume-preserving slip processes in metals. Hence, the volume of the solid material may be assumed constant beyond the yield point and the net change in volume of the simulation box may be attributed to void expansion alone (Gullett et al., 2004):

$$V_f=\frac{V_Y(1+\varepsilon_P)-V_{SY}}{V_Y(1+\varepsilon_P)}=\frac{(1+\varepsilon_P)-V_{SY}/V_Y}{(1+\varepsilon_P)}=\frac{f_0+\varepsilon_P}{1+\varepsilon_P}, \tag{6}$$

where ε_P represents the plastic strain, a strain level measured relative to the yield strain at which the volume of the solid and the whole system are denoted by V_Y and V_{SY}, respectively.

3. Results and discussion

3.1. Stress–strain response

We first performed atomistic simulations for systems containing a single void to study the void growth behavior under uniaxial strain. The geometry of the single void is of one-end-capped nanotube whose total length is three times its radius, as shown in Fig. 1(a). The system is then equilibrated for 50 ps under the microcanonical ensemble with temperature rescaling, followed by uniaxial expansion in a way described in Section 2. It is worth mentioning that due to fixed periodic box lengths along the non-loading dimensions, the induced stress state under uniaxial straining is non-uniaxial. To correlate a generally complex stress state with an equivalent uniaxial tensile loading path, the concepts of effective stress and strain are employed (Hosford, 2005). For the present case, the effective strain degenerates to the uniaxial strain since all other strain components are zero. A von Mises stress is calculated for each timestep and selected as the effective stress, which by definition is

$$\sigma_e=\sqrt{\tfrac{1}{2}[(\sigma_{11}-\sigma_{22})^2+(\sigma_{22}-\sigma_{33})^2+(\sigma_{33}-\sigma_{11})^2+6(\sigma_{12}^2+\sigma_{23}^2+\sigma_{31}^2)]}. \tag{7}$$

The effective stress–strain curves of the single-void model for four void sizes are shown in Fig. 3(a). All four curves exhibit a quasi-linear stress–strain behavior up to their yield points at which a substantial stress drop is observed. With a constant void fraction ratio of 0.5%, a size-dependent stress–strain behavior can be clearly observed from a variety of

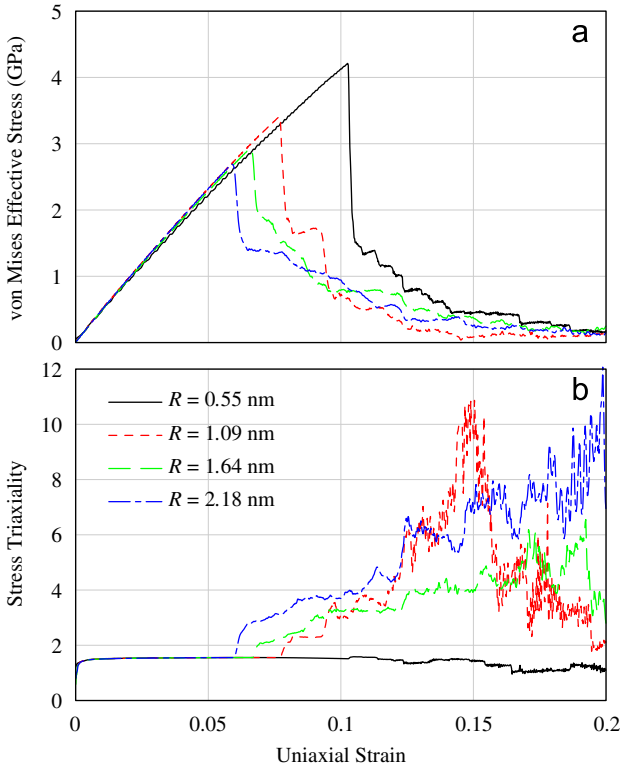

Fig. 3. The variation of (a) von Mises effective stress and (b) stress triaxiality for the four simulations of one-void model subjected to uniaxial strains up to 20%.

aspects. Firstly, the slope of the initial linear curves represents an increasing function of the simulation domain sizes. The larger the domain size, the higher the effective Young's modulus becomes. This behavior demonstrates that the size scale plays a role in the elastic deformation of systems containing nanovoids. Secondly, the critical (yield) stress and strain drop as the domain size increases: they are 4.21 GPa and 10.26% for $R=0.55$ nm and drop to 2.69 GPa and 5.9%, respectively, for $R=2.18$ nm. Moreover, the magnitude of the effective stress drop right beyond the yield point decreases with increasing domain sizes. For small domain sizes, dislocations generated from the void front are free to propagate to the boundaries of the simulation box before they have a chance to meet and interact with each other. As a direct result of the limit of the domain size, the work-hardening mechanism of the ductile aluminum is substantially weakened. As domain size increases, more and more dislocation reactions are allowed before they manage to reach the boundaries. Similar size-dependent behavior of the stress–strain response on domain sizes has previously been observed by Traiviratana et al. (2008) for copper and Potirniche et al. (2006) for nickel, respectively, despite their quite different void geometries. The size effects are also reflected in the other aspects of our atomistic simulations such as the binding energy per atom and the partial temperature calculated from the kinetic energy of all mobile atoms after excluding the x-dimensional velocity component.

Stress triaxiality, χ, is defined as the ratio of hydrostatic stress to the von Mises effective stress: $\chi=\sigma_h/\sigma_e$. It describes the portion of the stress tensor that is perpendicular to and on the octahedral plane. Hydrostatic stress is associated with the energy required to dilate a solid element. The von Mises effective stress is related to the distortion energy in view of its linear proportionality with the octahedral shear stress. Thus, stress triaxiality can physically be interpreted as the ratio between energies required to change the volume and shape of a solid element as it deforms. For a uniaxial strain test, the von Mises yield criterion yields the effective stress: $\sigma_e=2G\varepsilon$ with G representing the shear modulus. The corresponding hydrostatic stress is easy to calculate: $\sigma_h=K\varepsilon$ with K denoting the bulk modulus. For a numerical value of the stress triaxiality, the shear modulus can be estimated as the average of the lower $((C_{11}-C_{12})/2)$ and upper (C_{44}) bounds for single-crystal aluminum (Shukla, 1982) while the bulk modulus can be taken as $K=(C_{11}+2C_{12})/3$. Assuming the numerical values of the elastic stiffness constants by Meyers and Chawla (2009) for monocrystal aluminum at ambient temperature, a constant stress triaxiality of $\chi=K/2G\approx 1.46$ can be estimated for the linear elastic stage of the deformation. Fig. 3(b) shows the evolution of the stress triaxiality for the four simulations of the single-void model under uniaxial straining. Initially, the stress triaxiality rapidly ascends to the value of the theoretical prediction (≈ 1.46) for all simulations and subsequently remains constant until the yield point of each simulation is reached. The deviation of the triaxiality from 1.46 beyond the yield points is resulted from the continuous dislocation nucleation, propagation and interactions emanating from the void front. Dislocation initiation and movement with increasingly applied strain favors the shear deformation

while dislocation interaction hardens the material and makes the plastic slipping between neighboring close-packed planes more difficult. The complicated competing process results in the fluctuations in the stress triaxiality. In general, larger simulation runs experience higher triaxialities due to increased level of dislocation interactions.

3.2. Interpretation of yield stress from atomistic results using Gurson's model

One of the most frequently used models for studying the yielding condition for a continuous ductile medium containing microvoids is the one developed by Gurson (1977). The yielding function of the model is given as

$$\Phi = \frac{\sigma_e^2}{\sigma_Y^2} + 2f\cosh\left(\frac{3\sigma_h}{2\sigma_Y}\right) - 1 - f^2, \tag{8}$$

where f is the void volume fraction, σ_Y is the yield or flow stress of the virgin (unvoided) material and σ_h and σ_e are as usual denoting the hydrostatic and the von Mises effective stress. For uniaxial strain Gurson's yielding formulation can be rewritten as

$$\Phi = \frac{(2G\varepsilon)^2}{\sigma_Y^2} + 2f\cosh\left(\frac{K\varepsilon}{2\sigma_Y}\right) - 1 - f^2. \tag{9}$$

A conservative estimate of the yield stress, as suggested by Hosford (2005), assumes the maximum shear stress that can be sustained by a real crystal around $\frac{1}{10}$th of its shear modulus: $\tau_{max} \approx G/10$. Accordingly, a theoretical yield strength may be approximated as: $\sigma_Y = G/5$. This value, however, is orders of magnitude higher than the experimental measurements due to the generation, propagation and reaction of dislocations.

One interpretation predicated from Gurson's model is as follows: consider a homogenized (void-free) comparison material. In such a case, Gurson's model is simply the usual yield criterion:

$$\Phi = \frac{(2G\varepsilon)^2}{\sigma_Y^2} - 1. \tag{10}$$

Our goal, in order to interpret the atomistic calculations, is to find an "effective" yield stress σ_{Ye} of a material riddled with voids. Accordingly we equate Gurson's model with the above expression and compute σ_{Ye}:

$$\frac{(2G\varepsilon)^2}{\sigma_Y^2} + 2f\cosh\left(\frac{K\varepsilon}{2\sigma_Y}\right) - 1 - f^2 = \frac{(2G\varepsilon)^2}{\sigma_{Ye}^2} - 1. \tag{11}$$

We emphasize that σ_Y in Eq. (11) represents the microscopic yield stress of the corresponding unvoided material.

Fig. 4 shows the variation of critical stresses as a function of void size, predicted from both Gurson's yielding criterion and the atomistic calculations. As well-evident from the figure, Gurson's model (somewhat expected) fails to capture the size-effect in our atomistic calculations calling for the development of a modified Gurson's model. It is worth mentioning that the modification of Gurson's model (e.g. Wen et al., 2005) that accounts for gradient plasticity effects is not applicable in this particular size-regime since the characteristic length scales entering those formulations are in microns.

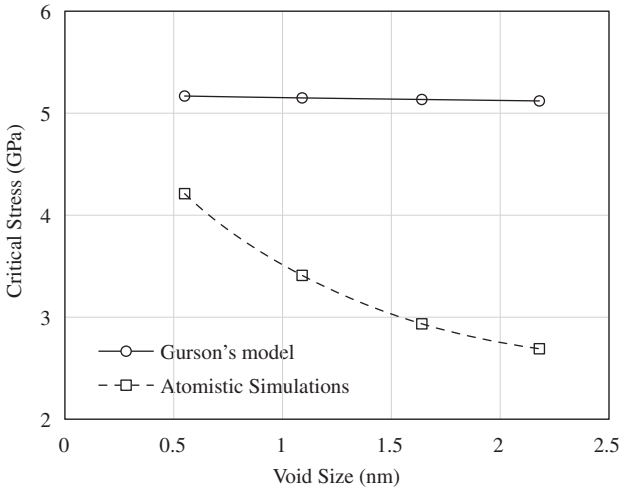

Fig. 4. Critical stresses predicted from atomistic simulations (dashed lines) and Gurson's continuum model (solid lines) as a function of void sizes for the four runs of one-void model.

3.3. Void growth mechanisms

It is mechanically well understood that fcc crystals deform by slip, which involves the sliding of one close-packed plane over another. As a result, slip generally affects the local atomic structures of two adjacent planes of atoms. (The plane on which the sliding of atoms occurs is called the slip plane and the direction of the sliding is known as slip direction.) For fcc crystals, slip naturally occurs on the close-packed {1 1 1} planes, on which the smallest possible Burgers vector is given by the smallest lattice vector, $\langle 1\,1\,0\rangle/2$. Such a perfect fcc dislocation, however, is not energetically favorable. Consider the specific case of an $(1\,1\,1)[1\,\bar{1}\,0]/2$ slip system. A dislocation with this Burgers vector may dissociate into two partial dislocations: $[1\,\bar{1}\,0]/2 \rightarrow [2\,\bar{1}\,\bar{1}]/6+[1\,\bar{2}\,1]/6$, by Frank's rule (Hirth and Lothe, 1982). This is the reason that perfect $\{1\,1\,1\}\langle 1\,1\,0\rangle/2$ dislocations are rarely observed in both experimental and atomistic studies. Nonetheless, they are still useful in calculating the favorable slip systems under given stress and strain states. The dissociation from a perfect dislocation into leading and trailing Shockley partial dislocations can subsequently be analyzed in terms of a Thompson tetrahedron (Hirth and Lothe, 1982). Under a general stress state ($\boldsymbol{\sigma}$), the resolved shear stress (RSS) of a slip system defined by a slip plane ($\mathbf{n}$) with the slip direction ($\mathbf{d}$) is given by

$$RSS = \mathbf{n}\cdot\boldsymbol{\sigma}\cdot\mathbf{d}. \tag{12}$$

For the uniaxial strain test of the single-void models with a small void fraction of 0.5%, $\sigma_{11} > \sigma_{22} \approx \sigma_{33}$ and all other stress components are approximately zero. The energetically favorable slip systems can then be summarized as: $(1\,1\,1)[1\,\bar{1}\,0]/2$, $(1\,1\,1)[1\,0\,\bar{1}]/2$, $(\bar{1}\,1\,1)[1\,0\,1]/2$, $(\bar{1}\,1\,1)[1\,1\,0]/2$, $(1\,\bar{1}\,1)[\bar{1}\,0\,1]/2$, $(1\,\bar{1}\,1)[\bar{1}\,\bar{1}\,0]/2$, $(1\,1\,\bar{1})[\bar{1}\,0\,\bar{1}]/2$, $(1\,1\,\bar{1})[\bar{1}\,1\,0]/2$, all with the same RSS of $(\sigma_{11}-\sigma_{22})/\sqrt{6}$. It is noted that, there are two equally favorable slip directions (edges of the Thompson tetrahedron) on each of the four close-packed slip planes (faces of the Thompson tetrahedron).

Fig. 5 shows the initiation, propagation and interaction of various dislocation structures for the largest run (1.08 million atoms) of the single-void model, as shown in Table 1 and Fig. 1(a). All the dislocation structures in the present paper are generated using the visual molecular dynamics package developed by Humphrey et al. (1996). Dislocation structures start to nucleate at the yield point (Fig. 3) around $t = 291$ ps, corresponding to a uniaxial strain of $\varepsilon = 5.82\%$ (Fig. 5(a)). Two shear loops on $(1\,1\,1)$ and $(1\,1\,\bar{1})$ planes are firstly nucleated (Fig. 5(b)). Each shear loop consists of two layers of atoms on its slip plane representing a partial annular stacking fault ribbon separating two Shockley partial dislocations. Both the leading and trailing

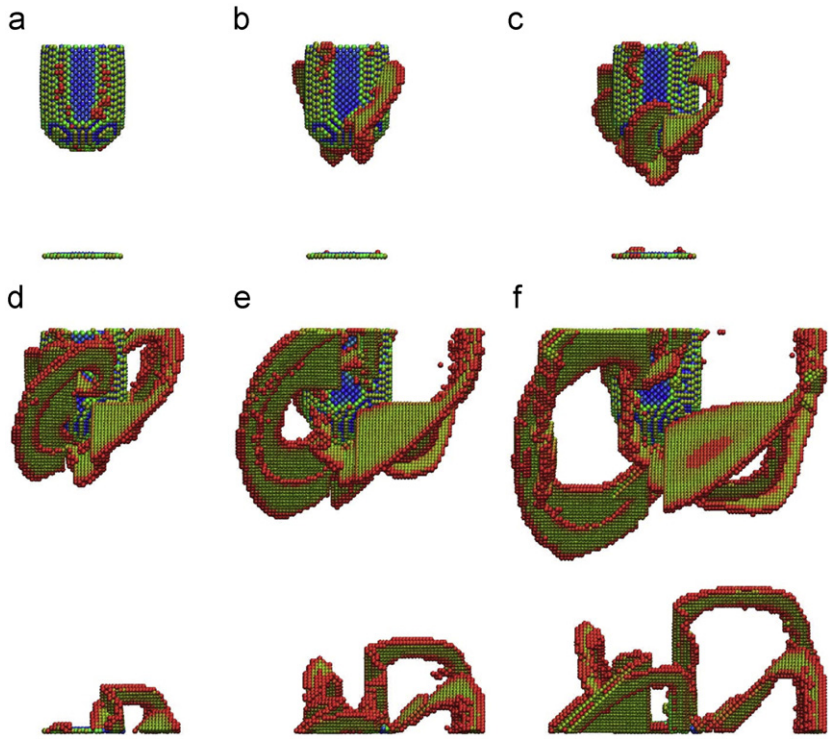

Fig. 5. Snapshots at the strain levels of (a) 5.82%, (b) 5.90%, (c) 5.94%, (d) 5.98%, (e) 6.02% and (f) 6.06% illustrating the nucleation, propagation and interactions of dislocation structures. Atom colors indicate various types of crystal defects according to the centro-symmetry deviation parameter: void front (blue), intrinsic stacking faults (green), Shockley partial dislocations (red) and Lomer–Cottrell stair-rod locks (yellow). Only atoms with a centro-symmetry deviation parameter greater than 0.5 are shown. (For interpretation of the references to color in this figure legend, the reader is referred to the web version of this article.)

partial dislocations are approximately bowed into semi-circles which are energetically favorable dislocation configurations due to the minimum stress required (Hirth and Lothe, 1982). As the uniaxial strain further increases more shear loops on various close-packed {1 1 1} planes are emitted from the void front. Notably, a newly generated shear loop on plane (1 1 1) propagates and meets with an existing shear loop on plane (1 1 $\bar{1}$). The direct product is the formation of a Lomer–Cottrell stair-rod lock (Fig. 5(c)). The possible reactions for the formation of Lomer–Cottrell dislocations are given by

$$[\bar{2}\ 1\ 1]/6+[1\ \bar{2}\ \bar{1}]/6=[\bar{1}\ \bar{1}\ 0]/6;\quad [1\ \bar{2}\ 1]/6+[\bar{2}\ 1\ \bar{1}]/6=[\bar{1}\ \bar{1}\ 0]/6. \tag{13}$$

It is seen that the Burgers vector of Lomer–Cottrell dislocations runs between centers of the Thompson tetrahedron faces and is out of any of the four slip planes. This makes the Lomer–Cottrell dislocation completely sessile and one of the major hardening mechanisms during plastic deformation. It hardens the material by preventing the associated shear loops from crossing each other and hence makes the subsequent plastic deformation more difficult. To accommodate the propagation of the two shear loops it borders, the Lomer–Cottrell dislocation extends its dislocation line under the application of increased strains (Fig. 5(d–f)). As the leading partial of the (1 1 1) shear loop expands, its trailing partial follows and gradually zips off the Lomer–Cottrell dislocation lock. More stacking fault ribbons, Lomer–Cottrell dislocations and other more complicated reactions are introduced as various shear loops propagate toward the boundaries of the simulation box. It is also interesting to observe the mutual repulsion between the shear loops and the rigid boundaries on which the uniaxial strains are applied (Fig. 5(e and f)). On the contrary, the shear loops are free to cross the periodic boundaries.

Another interesting aspect of the atomistic simulations involves the dynamical evolution of the void volume fraction. Based on the arguments presented in Section 2, the void fraction should approximately remain the same as its initial value (0.5%) until the yield point is reached, at which dislocation structures started to nucleate, propagate and interact. New vacant sites only develop during the stage of plastic deformations and are the direct cause of the tensile failure of ductile metals (Strachan et al., 2001). Fig. 6(a) shows the dynamical evolution of the void volume fraction for the four runs of the single-void model as a function of the overall uniaxial strain. The curves for the atomistic simulations are calculated from the algorithm developed in Section 2. As expected, no void expansions can be observed until critical strains are reached. Subsequently, the void fraction becomes roughly a linear function of strain and increases to a maximum value around 0.12. The size dependence behavior of void growth at this strain level ($\lesssim 20\%$) is consistent with the cylindrical voids expansion in nickel by Potirniche et al. (2006): an increasing void volume fraction is observed for smaller simulation domains due probably to their higher von Mises stresses, as shown in Fig. 3. The same conclusion can be drawn easily from Fig. 6(b) which is a replotting of Fig. 6(a) showing only the portions beyond the yield strains of each individual run. Even though the void expansion of smaller runs starts at a higher strain, the higher slope of their void fraction curves results in an increased void expansion at a final strain of 20%. Better linearity is achieved as the size of simulation domains increases. Also shown in Fig. 6(b) is the theoretical prediction of void fraction from Eq. (6), from which the quasi-linear dependence of void fraction on plastic strain becomes more clear in view of a Taylor series expansion of Eq. (6) for small plastic strains: $V_f=f_0+(1-f_0)\varepsilon_P-(1-f_0)\varepsilon_P^2+\cdots$. A reasonable agreement is confirmed between the atomistically calculated curves and the theoretical prediction. The evolution of the shape of the void for the largest run of the one-void simulation, say in the x–z plane after 7.5%, 10%, 15% and 20% of applied strain, are shown in Fig. 7.

As indicated in our introductory section, the works by Lubarda et al. (2004) and Traiviratana et al. (2008) proposed that voids grow through the mechanism of emission of shear dislocation loops. Bulatov et al. (2010) have challenged the validity of this assertion. In principle, shear loop emission cannot lead to void growth due to violation of mass conservation, however, in both ours as well as the simulations of Lubarda et al. (2004) and Traiviratana et al. (2008)

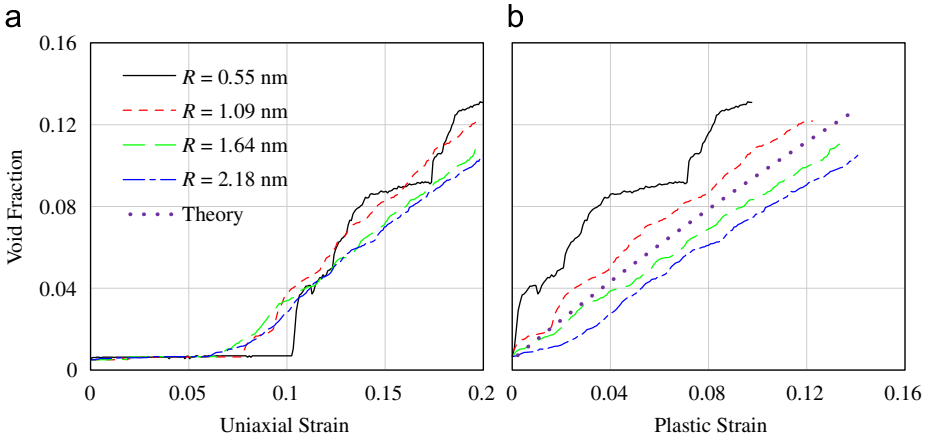

Fig. 6. The dynamical evolution of void volume fraction as a function of (a) uniaxial and (b) plastic strain for the four simulations of one-void model. The theoretical curve plotted in (b) is predicted by Eq. (6).

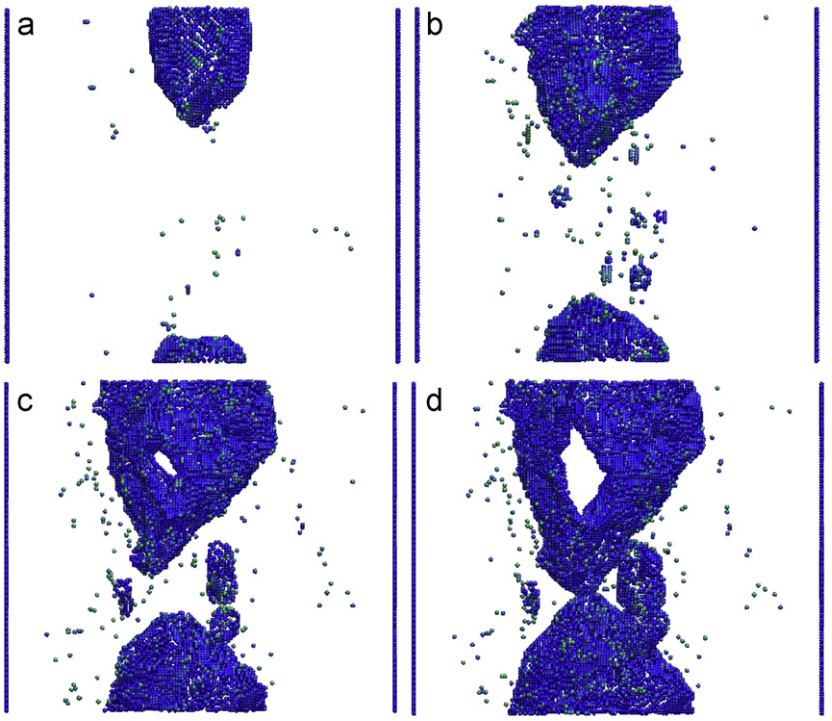

Fig. 7. Snapshots at (a) 7.5%, (b) 10%, (c) 15% and (d) 20% of applied strain illustrating the shape formed by the void front. Only atoms with a centro-symmetry deviation parameter greater than 17 are shown.

the beginning of emergence of shear loops are observed. We believe (as argued by Bulatov et al., 2010) that the shear loops observed in our simulations are initial stages of prismatic loop formation (which indeed can lead to void growth). Fig. 5 shows a completely detached prismatic loop observed in our simulations.

3.4. Void coalescence

To study the size effects and void fraction evolution under the influence of void coalescence, similar uniaxial straining tests are performed for specimens containing two voids and five voids under the same high strain rate of 2×10^8 s^{-1}. The size and distributions of voids for two-void and five-void models are illustrated in Fig. 1(b) and (c), respectively. With the initial void volume fraction kept the same (0.5%) for all three models, the size of voids decreases with an increased number of voids, as indicated in Table 1. For example, the sizes of the largest runs are 2.18, 1.73 and 1.28 nm for one-void, two-void and five-void models, respectively. Similar to the single-void simulations, several size-dependent behaviors including the effective stress–strain curve, stress triaxiality and void volume fraction are clearly observed across the four running cases for both two-void and five-void models. The same conclusions relevant to the size effects that have been drawn for the single-void model equally apply to the multi-void models. Instead, here we present a detailed comparison among the largest simulations of each individual model to concentrate on the effects of void distribution and coalescence.

Fig. 8(a) and (b) show the evolution of von Mises effective stress and stress triaxiality for the largest runs of the three models under uniaxial strains up to 20%. The corresponding simulation configurations are indicated in Fig. 1 and the last row of Table 1. Given the same number of atoms (1.08 million) and initial volume fraction (0.5%), the dependence of effective stresses on void distribution can clearly be observed. Initially, the slope of the quasi-linear elastic stress–strain curve slightly decreases with an increased number of voids. On the contrary, the five-void model exhibits the highest critical stress and strain. These observations demonstrate that at nanoscale void distribution plays a role in determining the deformation behavior of ductile metals. The same conclusion can be drawn from the evolution of stress triaxiality. The value deviates from the theoretical prediction of 1.46 at the individual critical points of the three curves. To better illustrate the effect of void distribution as well as that of simulation domain size, the critical stresses for all the twelve runs, four for each case, are tabulated in Fig. 9. While the critical stresses for all three cases decay with single-void size roughly following a power law, the vaster the void volume distribution the higher the critical stresses become. Also shown in the figure are corresponding critical yield stresses predicted from the continuum Gurson's model (Eq. (11)). Similar to the one-void case, the calculated critical yield stresses are fairly independent of both the single-void size and the void volume distribution and behave almost constant for all twelve runs.

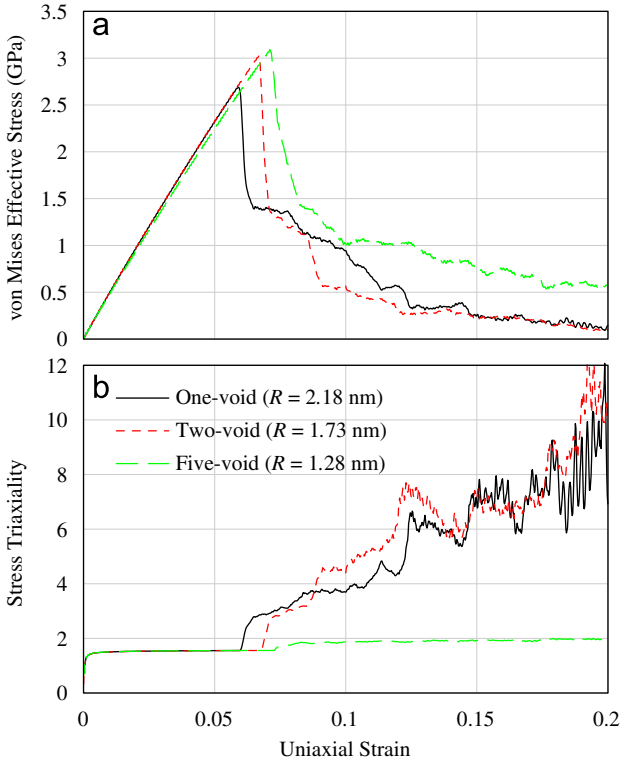

Fig. 8. The variation of (a) von Mises effective stress and (b) stress triaxiality for the largest runs of one-void, two-void and five-void models, respectively.

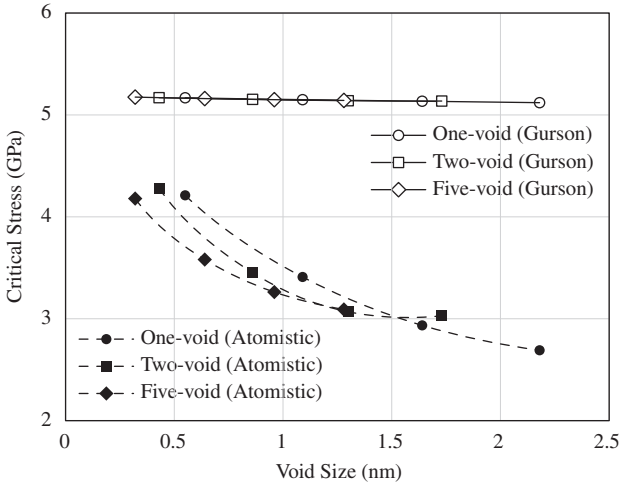

Fig. 9. Critical stresses predicted by atomistic simulations (dashed lines) and Gurson's continuum model (solid lines) as a function of void sizes for all runs of one-void, two-void and five-void models described in Table 1 and Fig. 1.

The stress–strain curves immediately after the stress drop are roughly overlapping for the one-void and two-void models, as shown in Fig. 8(a). This is due probably to the limited activities of dislocation interactions in the narrow ligament region between the two voids. The same overlapping behavior can be seen clearly in the stress triaxiality, as shown in Fig. 8(b). On the other hand, significant dislocation reactions are allowed in the wide region among the five voids, resulting in a universally elevated stress–strain curve in Fig. 8(a) and a suppressed triaxiality in (b).

Fig. 10 show the dislocation activity at several critical stages for the two-void (a)–(d) and five-void (e)–(h) specimens with the largest material lengths under uniaxial straining test. With the increase of uniaxial strains, red atoms first appear at the front of each void around the yield point (a) and (e) indicating the locales where the subsequent partial dislocations are about to emit. Up to this strain level, all deformations are seen to be elastic. The aspect ratio of individual voids is directly proportional to the uniaxial strain with the long axis of each void aligned along the loading direction. As the

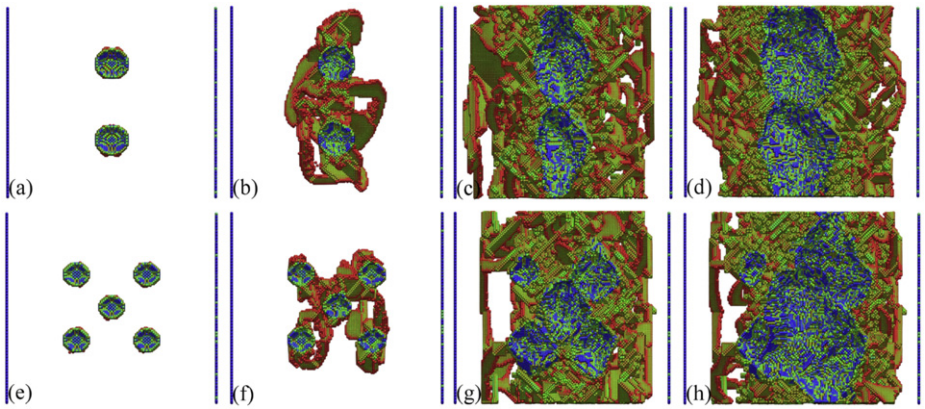

Fig. 10. Snapshots showing the morphological evolution of void coalescence for the largest runs of two-void model (first row) at strain levels of (a) 6.36%, (b) 6.76%, (c) 10.00% and (d) 20.00% and five-void model (second row) at (e) 7.02%, (f) 7.18%, (g) 8.98% and (h) 20.00% under uniaxial strain. Atoms are colored according to the centro-symmetry deviation parameter. Only atoms with a centro-symmetry deviation parameter greater than 0.5 are shown. (For interpretation of the references to color in this figure legend, the reader is referred to the web version of this article.)

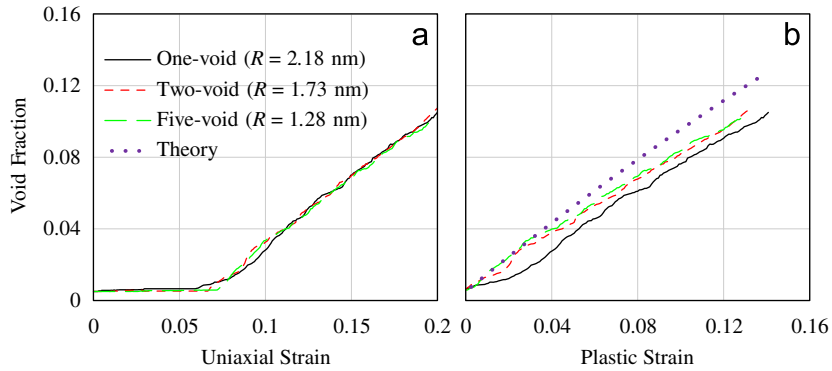

Fig. 11. The dynamical evolution of void volume fraction as a function of (a) uniaxial and (b) plastic strain for the largest runs of one-void, two-void and five-void models. Also shown in (b) is the theoretical void fraction predicted by Eq. (6).

applied strain keeps increasing, shear loops nucleated from neighboring voids propagate and interact (b) and (f). This stage corresponds to the large stress drops right beyond the yield points in Fig. 8(a). A large amount of strain energies stored within the simulation domains due to uniaxial strains are dissipated by the various dislocation motions. The aspect ratio of individual voids have been gradually reversed under the increased level of plastic deformations (c) and (g). As a result, initially separated voids have been brought together and coalesce into a single and larger void. This stage roughly corresponds to the end of the large stress drops in Fig. 8(a). Further application of the uniaxial strains up to 20% continuously weakens the load-carrying capacity of the specimens and substantially increases the volume of the coalesced void (d) and (h).

Shown in Fig. 11 is the dynamical evolution of the void volume fraction as a function of overall uniaxial strain and plastic strain for the largest runs of one-, two- and five-void models. As in the case of the single-void simulations, the volume fraction remains roughly the same as the initial value of 0.5% until the yield points are reached, as shown in Fig. 11(a). Although the void fractions of individual runs start to grow at their own yield points, they end up with roughly the same value of 0.11 at the final uniaxial strain of 20%, as shown in Fig. 11(b). Surprisingly, no obvious void coalescence is observed for the two-void and five-void void growth curves. For example, there is no significant increase in void growth in the vicinity of multiple voids coalescing into a single void and all three curves reasonably follow the theoretical prediction by Eq. (6). This observation, however, is consistent with the cylindrical void growth mechanism in nickel investigated by Potirniche et al. (2006), in which effect is attributed to the very high strain rate effects intrinsically associated with molecular dynamics simulations.

4. Concluding remarks

Molecular dynamics simulations have been performed to investigate the mechanism of void growth and coalescence in aluminum, with particular emphasis on the dislocation analysis. Simulations consisting of several tens of thousands to

over a million atoms, at four different material lengths, reveal a clear size dependence of load-carrying capacity during a uniaxial tension test. Multi-void specimens with the same initial void fraction are employed to study the effects of void distribution and coalescence. Given the very high strain rate that is intrinsically associated with atomistic simulations, the main observations are as follows:

1. For all simulation cases, deformation prior to yield points exhibits quasi-linear elasticity. A length scale effect is clearly indicated by the effective stress–strain response as well as stress triaxiality. The larger the simulation domain size the lower the yield stress and strain become. Gurson's model (Gurson, 1977) fails to capture the observed size-effect and calls for its modification accounting for the mechanisms prevalent at the nanoscopic void dimensions.
2. Void volume fraction remains a constant until the critical stresses are reached. Void grows and coalesces by the continuous nucleation, propagation and reaction of shear loops emitted from void front. All energetically favorable fcc $\{1\,1\,1\}\langle 1\,1\,\overline{2}\rangle/6$ partial slip systems are observed under external forces. A shear loop typically consists of two Shockley partial dislocations bounding a stacking fault ribbon in between. Lomer–Cottrell stair-rod sessile dislocations are formed by the reaction of two Shockley partial dislocations from intersecting slip planes. Rigid boundaries produce repulsive forces on propagating dislocations. The forces divert dislocations to propagate toward the periodic boundaries instead of the rigid ones.
3. A void growth algorithm based on simple-cubic discretization of the rectangular simulation domains is proposed and implemented to characterize the void expansion. Under uniaxial strains up to 20%, a small size dependence of void fraction evolution is observed. A smaller simulation domain results in higher void volume fraction at the end of the straining test. Nonetheless, void fractions from all four material lengths show a reasonable agreement with the theoretical prediction deduced from geometric arguments.
4. Under the condition of constant void fraction, multi-void specimens generally result in higher yield stresses and elevated load-carrying capacity than single-void samples through more intensive dislocation interactions. This observation demonstrates that the stress resistivity of specimens can be enhanced by redistributing a large void into multiple small ones at nanoscale. The evolution of void fraction, however, seems to be independent of the number of voids given a constant void fraction. No obvious acceleration of void expansion due to coalescence of neighboring voids are recorded.

Acknowledgments

We acknowledge the financial support from U.S. DOD Contract DODAF41611. We would like to express our sincere gratitude to Professor Karl Sieradzki (Arizona State University) for his enlightening comments and discussions. Pradeep Sharma was funded by AFOSR FA9550-09-1-0200 (Program Manager: Ali Sayir).

References

Admal, N.C., Tadmor, E.B., 2010. A unified interpretation of stress in molecular systems. Journal of Elasticity 100, 63–143.
Andersen, O.K., 1975. Linear methods in band theory. Physical Review B 12, 3060–3083.
Belak, J., Minich, R., 1998. Simulation of void growth at high strain-rate. Materials Research Society Proceedings 539, 257–261.
Bringa, E.M., Lubarda, V.A., Meyers, M.A., 2010. Response to "shear impossibility: comments on 'Void growth by dislocation emission' and 'Void growth in metals: atomistic calculations'". Scripta Materialia 63, 148–150.
Bulatov, V.V., Wolfer, W.G., Kumar, M., 2010. Shear impossibility: comments on "Void growth by dislocation emission" and "Void growth in metals: atomistic calculations". Scripta Materialia 63, 144–147.
Cuitino, A.M., Ortiz, M., 1996. Ductile fracture by vacancy condensation in fcc single crystals. Acta Metallurgica et Materialia 44, 427–436.
Daw, M.S., Baskes, M.I., 1983. Semiempirical, quantum mechanical calculation of hydrogen embrittlement in metals. Physical Review Letters 50, 1285–1288.
Daw, M.S., Baskes, M.I., 1984. Embedded-atom method: derivation and application to impurities, surfaces and other defects in metals. Physical Review B 29, 6443–6453.
Dufek, E.J., Seegmiller, J.C., Bazito, R.C., Buttry, D.A., 2007. Dioxygen reduction affects surface oxide growth and dissolution on AA2024-T3. Journal of the Electrochemical Society 154, C458–C464.
Foiles, S.M., Daw, M.S., Baskes, M.I., 1986. Embedded-atom method functions for the fcc metals Cu, Ag, Au, Ni, Pd, Pt, and their alloys. Physical Review B 33, 7983–7991.
Fontana, M.G., 1986. Corrosion Engineering. McGraw-Hill, New York.
Gullett, P.M., Wagner, G., Slepoy, A., 2004. Numerical tools for atomistic simulations. Sandia Report, SAND2003-8782, Sandia National Laboratories.
Gurson, A.L., 1977. Continuum theory of ductile rupture by void nucleation and growth: part I—yield criteria and flow rules for porous ductile media. Journal of Engineering Materials and Technology 99, 2–15.
Hirth, J.P., Lothe, J., 1982. Theory of Dislocations. John Wiley and Sons, New York.
Hosford, W.F., 2005. Mechanical Behavior of Materials. Cambridge University Press, Cambridge.
Humphrey, W., Dalke, A., Schulten, K., 1996. VMD—visual molecular dynamics. Journal of Molecular Graphics 14, 33–38.
Jang, I., Burris, D.L., Dickrell, P.L., Barry, P.R., Santos, C., Perry, S.S., Phillpot, S.R., Sinnott, S.B., Sawyer, W.G., 2007. Sliding orientation effects on the tribological properties of polytetrafluoroethylene. Journal of Applied Physics 102, 123509.
Kelchner, C.L., Plimpton, S.J., Hamilton, J.C., 1998. Dislocation nucleation and defect structure during surface indentation. Physical Review B 58, 11085–11088.
Li, J., Krystyn, J., Vliet, V., Zhu, T., Yip, S., Suresh, S., 2002. Atomistic mechanisms governing elastic limit and incipient plasticity in crystals. Nature 418, 307–310.
Lubarda, V.A., Schneider, M.S., Kalantar, D.H., Remington, B.R., Meyers, M.A., 2004. Void growth by dislocation emission. Acta Materialia 52, 1397–1408.
Lubarda, V.A., 2011. Emission of dislocations from nanovoids under combined loading. International Journal of Plasticity 27, 181–200.

Marian, J., Knap, J., Ortiz, M., 2004. Nanovoid cavitation by dislocation emission in aluminum. Physical Review Letters 93, 165503.
Mcclintock, F.A., Argon, A.S., Backer, S., 1966. Mechanical Behavior of Materials. Addison-Wesley Publishing Co., Reading, MA.
Meyers, M.A., Chawla, K.K., 2009. Mechanical Behavior of Materials. Cambridge University Press, Cambridge.
Mishin, Y., Farkas, D., Mehl, M.J., Papaconstantopoulos, D.A., 1999. Interatomic potentials for monoatomic metals from experimental data and ab initio calculations. Physical Review B 59, 3393–3407.
Onck, P.R., van der Giessen, E., 1999. Growth of an initially sharp crack by grain boundary cavitation. Journal of the Mechanics and Physics of Solids 47, 99–139.
Pei, Q., Lu, C., Liu, Z., Lam, K., 2007. Molecular dynamics study on the nanoimprint of Coppor. Journal of Physics D: Applied Physics 40, 4928–4935.
Plimpton, S.J., 1995. Fast parallel algorithms for short-range molecular dynamics. Journal of Computational Physics 117, 1–19.
Potirniche, G., Horstemeyer, M., Wagner, G., Gullett, P., 2006. A molecular dynamics study of void growth and coalescence in single crystal nickel. International Journal of Plasticity 22, 257–278.
Rudd, R.E., Seppala, E.T., Dupuy, L.M., Belak, J., 2007. Void coalescence processes quantified through atomistic and multiscale simulation. Journal of Computer-Aided Materials Design 14, 425–434.
Rudd, R.E., 2009. Void growth in bcc metals simulated with molecular dynamics using the Finnis–Sinclair potential. Philosophical Magazine 89, 3133–3161.
Scheyvaerts, F., Onck, P.R., Tekoğlu, C., Pardoen, T., 2011. The growth and coalescence of ellipsoidal voids in plane strain under combined shear and tension. Journal of the Mechanics and Physics of Solids 59, 373–397.
Shen, Y-L., 2004. On the atomistic simulation of plastic deformation and fracture in crystals. Journal of Materials Research 19, 973–976.
Shukla, M.M., 1982. The shear bounds of the cubic polycrystal and its experimental shear modulus. Journal of Physics D: Applied Physics 15, L177–L180.
Strachan, A., Cagin, T., Goddard III, W.A., 2001. Critical behavior in spallation failure of metals. Physical Review B 63, 060103.
Subramaniyan, A.K., Sun, C., 2008. Continuum interpretation of virial stress in molecular simulations. International Journal of Solids and Structures 45, 4340–4346.
Traiviratana, S., Bringa, E.M., Benson, D.J., Meyers, M.A., 2008. Void growth in metals: atomistic calculations. Acta Materialia 56, 3874–3886.
Tvergaard, V., 1990. Material failure by void growth to coalescence. Advances in Applied Mechanics 27, 83–151.
Tvergaard, V., Needleman, A., 1995. Effects of nonlocal damage in porous plastic solids. International Journal of Solids and Structures 32, 1063–1077.
van der Giessen, E., Tvergaard, V., 1990. On cavity nucleation effects at sliding grain boundaries in creeping polycrystals. In: Wilshire, B., Evans, R.W. (Eds.), Proceedings of the Fourth International Conference on "Creep and Fracture of Engineering Materials and Structures". Pineridge Press, Swansea, pp. 169–178.
Wei, S.H., Krakauer, H., 1985. Local-density-functional calculation of the pressure-induced metallization of base and bate. Physical Review Letters 55, 1200–1203.
Wen, J., Huang, Y., Hwang, K.C., Liu, C., Li, M., 2005. The modified Gurson model accounting for the void size effect. International Journal of Plasticity 21, 381–395.
Zhao, K.J., Chen, C., 2008. Atomistic modeling size dependence of nano-voided Copper yielding under uniaxial tension. In: Advances in Heterogeneous Material Mechanics 2008—Proceedings of the Second International Conference on Heterogeneous Material Mechanics, pp. 338–341.
Zimmerman, J.A., Kelchner, C.L., Klein, P.A., Hamilton, J.C., Foiles, S.M., 2001. Surface step effects on nanoindentation. Physical Review Letters 87, 165507.